

# SCIENTIFIC REPORTS



OPEN

## Empirical Models of Shear-Wave Radiation Pattern Derived from Large Datasets of Ground-Shaking Observations

Sreeram Reddy Kotha<sup>1,2</sup>, Fabrice Cotton<sup>1,2</sup> & Dino Bindi<sup>1</sup>

Shear-waves are the most energetic body-waves radiated from an earthquake, and are responsible for the destruction of engineered structures. In both short-term emergency response and long-term risk forecasting of disaster-resilient built environment, it is critical to predict spatially accurate distribution of shear-wave amplitudes. Although decades' old theory proposes a deterministic, highly anisotropic, four-lobed shear-wave radiation pattern, from lack of convincing evidence, most empirical ground-shaking prediction models settled for an oversimplified stochastic radiation pattern that is isotropic on average. Today, using the large datasets of uniformly processed seismograms from several strike, normal, reverse, and oblique-slip earthquakes across the globe, compiled specifically for engineering applications, we could reveal, quantify, and calibrate the frequency-, distance-, and style-of-faulting dependent transition of shear-wave radiation between a stochastic-isotropic and a deterministic-anisotropic phenomenon. Consequent recalibration of empirical ground-shaking models dramatically improved their predictions: with isodistant anisotropic variations of  $\pm 40\%$ , and 8% reduction in uncertainty. The outcomes presented here can potentially trigger a reappraisal of several practical issues in engineering seismology, particularly in seismic ground-shaking studies and seismic hazard and risk assessment.

A seismic ground-shaking map predicts the spatial distribution of the shaking intensity in the nearby geographic area. Rapidly generated ground-shaking maps for a single event, such as the USGS ShakeMaps<sup>1</sup>, have become invaluable for public information, damage assessment, emergency responses, and engineering and scientific analyses. While ground-shaking maps for several thousand prospective earthquakes are required for probabilistic seismic hazard and risk assessment of spatially extended infrastructures. Such predictions combine the information on earthquake magnitude, geometry, and location with a ground-shaking prediction model, to estimate ground-shaking intensities (typically in terms of Pseudo-Spectral Acceleration, PSA) over a wide area around the epicenter. Often, empirical prediction models are developed for regions with sufficient ground-shaking data (e.g., recorded seismograms), while in regions with sufficient tectonic and geological information, physics based numerical simulations are preferred. Nevertheless, the practicality of seismic hazard and risk assessment is only as good as the underlying ground-shaking prediction model, especially in their description of the spatial variability of seismic wave amplitudes (in this study, PSAs).

S-waves, as the elastic shear-waves, are the strongest seismic (body) waves, and are responsible for shaking and damaging of man-made structures. Most empirical ground-shaking models are derived to predict the scaling of S-wave amplitudes with earthquake moment magnitude ( $M$ ), and its distance from the affected site ( $R$ ). Coupling the largest datasets<sup>2,3</sup> and numerical simulations, recent ground-shaking prediction models<sup>4,5</sup> have achieved considerable explanatory and predictive power. Despite being intuitive and computationally efficient, empirical ground-shaking models have one major limitation; these models assume and predict the radiation pattern of S-wave energy to be isotropic. This is far from reality, because a double-couple shear dislocation (e.g., an earthquake) radiates energy very differently from an explosive/implosive dislocation (e.g., a bomb).

<sup>1</sup>Helmholtz Centre Potsdam, GFZ German Research Centre for Geosciences, 14467, Potsdam, Germany. <sup>2</sup>University of Potsdam, Potsdam, Germany. Correspondence and requests for materials should be addressed to S.R.K. (email: sreeram@gfz-potsdam.de)

The theoretical formulation<sup>6</sup> of S-wave radiation patterns is anisotropic yet deterministic, and depends on the rupture geometry and focal mechanism. Empirically<sup>7–10</sup> though, S-wave radiation patterns transition between deterministic and stochastic depending on the heterogeneity of propagation medium, which makes it difficult to calibrate and include in prediction models. Consequently, both numerical and empirical prediction models suffer from either miscalibration or oversimplification of the S-wave radiation phenomenon.

### Elusive S-Wave Radiation Patterns

A vertically dipping strike-slip earthquake in a homogenous half-space radiates S-wave energy as a four-lobed pattern: with the largest S-wave amplitudes in the rupture strike and normal directions ( $0^\circ, \pm 90^\circ, 180^\circ$ ), and relatively lower amplitudes elsewhere. Some empirical analyses<sup>7–10</sup> have reported large isodistant azimuthal variations of S-wave amplitudes around the epicenters of various strong earthquakes, which suggested the need to include realistic radiation patterns into empirical<sup>11</sup> and numerical prediction models. However, unlike their theoretical formulation, radiation patterns are observable only in a limited bandwidth of S-wave frequencies and in a limited epicentral distance range<sup>12,13</sup>. For some earthquakes<sup>8,14</sup>, the four-lobed S-wave radiation pattern was observed to be intact at frequencies as high as 16 Hz. While for others<sup>7,15</sup>, the four-lobes were completely disrupted by small-scale crustal heterogeneities<sup>12,16</sup> beyond frequencies as low as 4 Hz. The mixing of SH–SV wave polarities during propagation in a layered crustal medium<sup>15,17</sup> appears to distort the four-lobed pattern as well.

Regarding the frequency-dependence, S-wave radiation appears to transition from a deterministic to a stochastic process around frequencies of 1–4 Hz. Numerical simulations<sup>17</sup> of wave propagation in randomized three-dimensional crustal velocity models have been able to reproduce this transitional range, but of course, the results are sensitive to the parametric description of crustal scattering properties (e.g., correlation length of medium heterogeneities). Based on observations and simulations, a few others<sup>18,19</sup> elaborated and applied analytical models depicting a smooth, linear transition between anisotropic and isotropic radiation patterns in the frequency range 1–3 Hz, in order to study earthquake source and propagation effects.

In most studies related to S-wave radiation pattern, despite differences in underlying methodologies, the equally essential distance-dependence of radiation pattern is often ignored. Studies<sup>20,21</sup> based on observed energy partitioning of S-waves revealed a very weak distance dependency for frequencies 2–5 Hz, and distance independent isotropic pattern beyond 6 Hz – but the dataset consisted of only three earthquakes recorded in the distance range 13–27 km. A more recent study<sup>13</sup> based on observed spatial distribution of maximum amplitudes, used a larger dataset consisting of 13 strike-slip earthquakes (in Chugoku region, Japan) recorded in 0–150 km distance range. The resulting empirical model<sup>13</sup> captures both frequency- and distance-dependence, wherein the cross-correlation coefficient between observed and theoretical low frequency S-wave (0.5–1 Hz) amplitudes decreases linearly (from 0.75) beyond a normalized hypocentral distance  $\log(kL) \sim 1.64$ , which is approximately 30 km when wave number  $k = 1.33 \text{ km}^{-1}$ . While a few earlier studies<sup>12,22</sup> suggested that four-lobed pattern remains intact up to 40 km, even for high frequencies ( $>4 \text{ Hz}$ ). Essentially, a good understanding, and robust empirical models of the frequency- and distance-dependent S-wave radiation pattern are sought.

Although there is a reasonable agreement across all these studies, we observe that most are based on rather small datasets consisting of few (predominantly) strike-slip events. In addition, we identify that: (1) the frequency range (e.g. 1–3 Hz) wherein the transition appears to occur, needs to be evaluated, (2) the datasets were rather limited in terms of magnitude and distance ranges, and diversity of style-of-faulting (i.e. strike, reverse, normal, and oblique-slip events), and (3) most analyses were performed in the Fourier domain, which limits their adoption in engineering applications relying heavily on PSA (Pseudo-Spectral Acceleration) predictions<sup>23,24</sup>. In this study, we tackle these limitations using the recently published large datasets compiled of several thousand seismograms, from a variety of earthquake focal-mechanisms, occurring across the globe, and uniformly processed specifically for engineering applications i.e., code<sup>23,24</sup> based design of earthquake resistant structures.

Even with such large datasets derived from spatially dense strong-motion networks in Japan<sup>25</sup> and southern California, USA<sup>26</sup>, the imprint of S-wave radiation pattern remained untraceable and unquantifiable within the mixed-effects regression based empirical ground-shaking models<sup>11</sup>. Understandably, radiation pattern is a *secondary* physical effect masked by other dominant physical processes, including: geometric spreading and anelastic attenuation with distance, scaling with event magnitudes and event-to-event variability of rupture dynamics, and the strong influence of local soil conditions at a recording surface site. These difficulties explain why the well-known four-lobed S-wave radiation pattern has never been taken into account in the development of PSA predicting Ground-Motion Prediction Equations<sup>11</sup>. However, most surface sites with stiff layers of top-soil<sup>23,24</sup> and the overlying man-made structures<sup>27</sup> resonate with a fundamental frequency from 0.2 Hz to 5 Hz, which coincides with the frequency range where the anisotropy of S-wave energy distribution is most prominent<sup>28</sup>. Therefore, it is critical that the spatial anisotropy of S-wave radiation pattern is incorporated into Ground-Motion Prediction Equations<sup>11</sup> – the fundamental components of Probabilistic Seismic Hazard Assessments and rapidly deployable ground-shaking maps.

### Empirical Evidence of S-Wave Radiation Patterns

In our recent studies<sup>29,30</sup>, we tackled the various assumptions and limitations in development of mixed-effects regression based empirical ground-shaking models. Taking advantage of recently published large datasets<sup>2,3,31</sup> and mixed-effects regression analyses<sup>32</sup>, we systematically quantified and isolated the dominant physical processes that control the spatial variability of ground-shaking. In the present study, we have gone a step further to analyze the *left-over* regression residuals, those quantifying the record-to-record variability of observed ground-shaking, from two empirical ground-shaking models<sup>33,34</sup> (equation 1) developed from two recently compiled datasets<sup>2,3</sup> of active shallow crustal earthquake recordings: one<sup>3</sup> from the Japanese KiK-net<sup>25</sup> strong-motion network; and another as a global NGA-West2 dataset<sup>2</sup> compiled mostly of events from southern California<sup>26</sup> (USA), plus a

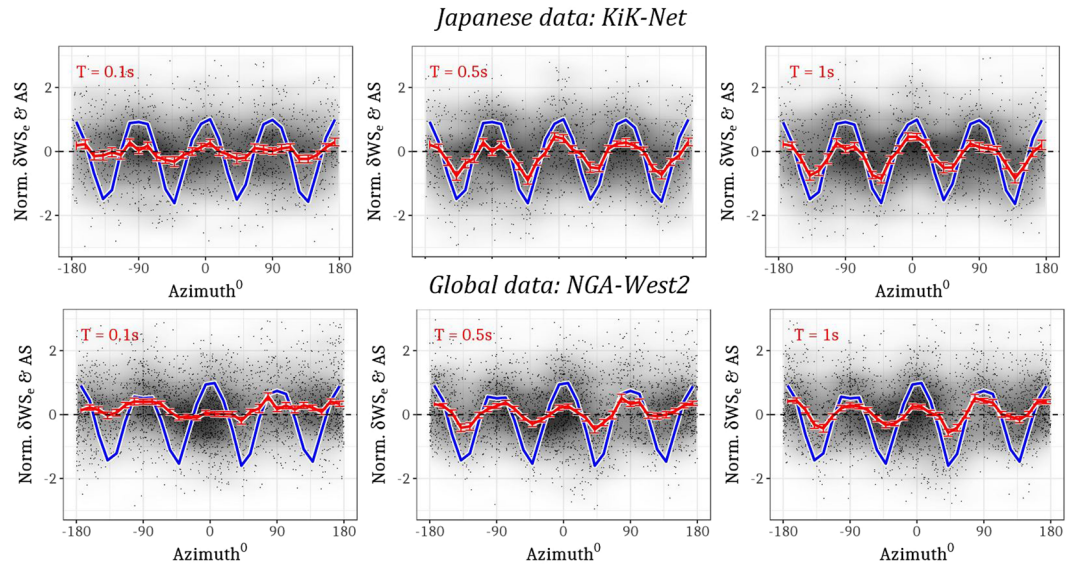


**Figure 1.** Empirical evidence of S-wave radiation patterns in residuals from records at  $R \leq 100$  km for strike-slip events in Japan: KiK-net (top) and Global: NGA-West2 (bottom) datasets. Panels show normalized residual  $\delta WS_{e,s}$  (black) and binned mean of normalized  $\delta WS_{e,s}$  (red) extracted from mixed-effects regression of PSAs with  $T = 0.1$  s,  $0.5$  s,  $1$  s (left to right), and binned means of normalized, theoretical far-field S-wave amplitudes (blue) corresponding to each record.

few large events from Italy, Taiwan, Turkey, China, Alaska, Georgia, Montenegro, New Zealand, and other active seismic regions.

$$\ln(\text{PSA}) = f_R(M, R) + f_M(M) + \delta B_e + \delta S2S_s + \delta WS_{e,s} \quad (1)$$

The most common expression of S-wave amplitudes used in engineering seismology and earthquake engineering is an average<sup>35</sup> of two-component (i.e., NS, EW) horizontal PSAs, for a range of spectral periods (e.g.  $T = 0.01$ – $10.0$  s). All of the ground-shaking datasets<sup>2,3</sup> disseminate the observed ground-shaking intensity data only in terms of PSAs. The two ground-shaking models<sup>33,34</sup> we considered were also developed to predict PSAs, because most seismic design codes<sup>23,24</sup> rely on predicted PSAs. PSAs are essentially the peak acceleration responses to seismic excitation (i.e., a seismogram) of a suite of viscous damped (5% or other) single-degree-of-freedom oscillators with fundamental frequencies  $f_{osc} = \frac{1}{T}$ . It is true that conversion of ‘as recorded’ Fourier amplitudes to ‘engineering purposed’ PSAs is nonlinear<sup>36</sup>, which often makes the physical interpretations made in either of the domains non-interchangeable. However, within the earthquake moment magnitude ( $M_{3.4}$ – $M_{6.9}$ ) and period range of interest in this study ( $T = 0.1$ – $1.0$  s), responses of a single-degree-of-freedom (i.e., the PSAs) are dominated by the Fourier amplitudes of S-wave frequencies around  $f_{osc}$ <sup>36</sup>. Hence, we can interpret the radiation pattern effects in PSA residuals as Fourier spectral features of the seismic input.

Typically, empirical ground-shaking prediction models (e.g., equation 1) are regressed from datasets of observed PSAs at several surface sites from multiple past earthquakes in a region. In equation (1), the fixed-effect  $f_R(M, R)$  captures the geometric spreading and apparent anelastic attenuation of PSAs with rupture moment magnitude ( $M$ ) and distance to site ( $R$ ), and  $f_M(M)$  captures the scaling of PSAs with  $M$ .  $\delta B_e$  and  $\delta S2S_s$  are the random-effects quantifying event-to-event (event index  $e$ ) and site-to-site (surface site index  $s$ ) variabilities, respectively. The left-over record-specific residuals  $\delta WS_{e,s}$  (of event  $e$  recorded at surface site  $s$ ) contain all of the phenomena that evade the fixed- and random-effects, including the four-lobed S-wave radiation pattern. For brevity, we refer interested readers to the articles<sup>33,34</sup> elaborating on the ground-shaking model development.

Figure 1 presents the empirical evidence of S-wave radiation patterns in ground-shaking data (i.e., residuals  $\delta WS_{e,s}$ ). While the most recent studies<sup>13,22</sup> considered 13 events, we select 1615 and 3193  $\delta WS_{e,s}$  residuals (records) at  $R \leq 100$  km of 91 and 78 strike-slip events from the KiK-net<sup>3</sup> and NGA-West2<sup>2</sup> datasets, respectively. These residuals are standardized i.e., divided by their standard deviation ( $\phi_0$ ), and plotted against the azimuth of the recording stations measured with respect to the rupture strike direction. As no single event is recorded by a complete  $360^\circ$  and  $0$  km to  $100$  km network, by re-orienting the 142 and 299 surface site locations (of KiK-net and NGA-West2, respectively) to the rupture strike as datum, the radiation pattern can be seen as an average trend over several dozen earthquakes of size  $M_{3.0}$ – $M_{6.0}$  (Fig. 1, red curve). The four-lobed radiation pattern of a vertical dipping strike-slip event produces greater than average ground-shaking (over all azimuths) in the strike parallel and normal directions (azimuth =  $0^\circ, \pm 90^\circ, \pm 180^\circ$ ), and the weakest ground-shaking in between (azimuth =  $\pm 45^\circ, \pm 135^\circ$ ). The red curve in Fig. 1 represents the binned means of the standardized  $\delta WS_{e,s}$  residuals, and shows a clear trend that is characteristic of the expected four-lobed radiation pattern.

An important point regarding the data selection is that, we did not specifically identify and remove the records (and corresponding  $\delta WS_{e,s}$ ) with possible directivity effects. A recent study<sup>37</sup> showed that a few small-moderate



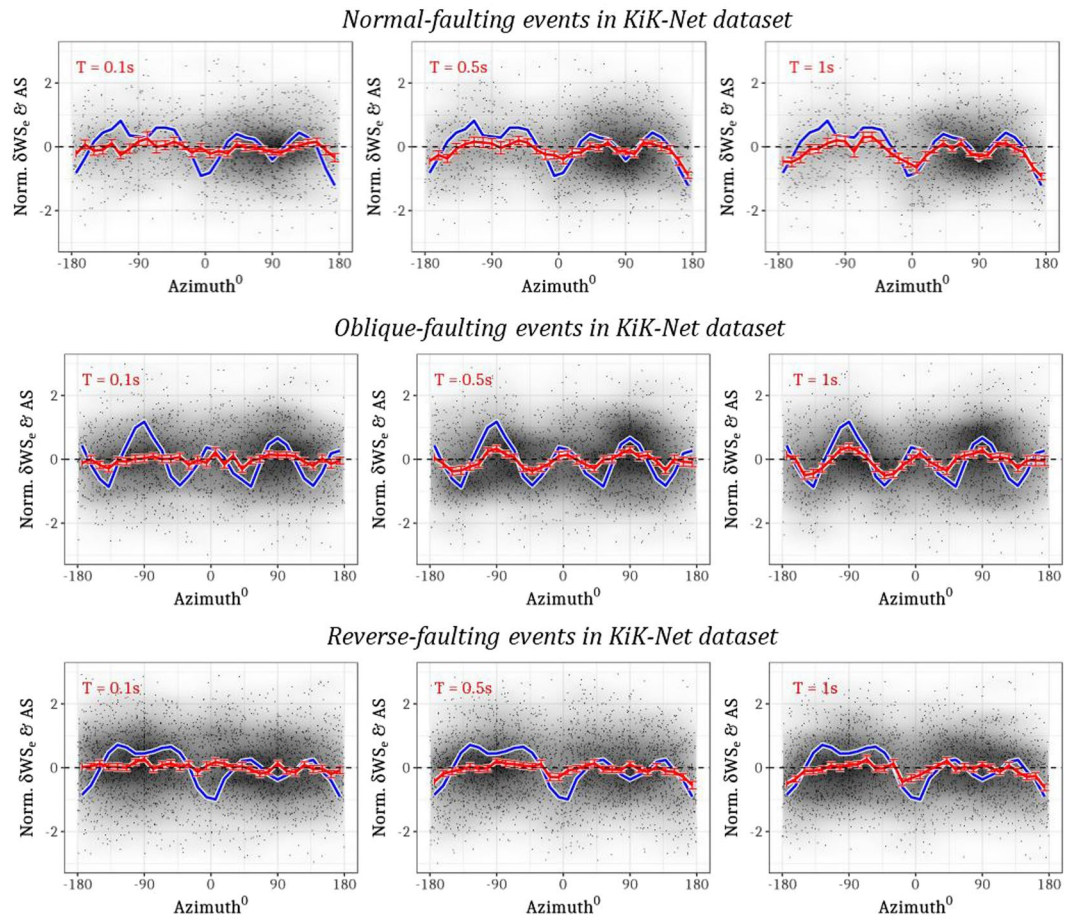


**Figure 2.** Empirical evidence of S-wave radiation patterns in residuals from records at  $R \leq 100$  km of normal, oblique, and reverse-slip events (top to bottom) from the Japanese KiK-net dataset. The panels show the normalized residuals  $\delta WS_{e,s}$  (black), binned means of normalized residuals  $\delta WS_{e,s}$  (red), and binned means of normalized, theoretical S-wave amplitudes (blue) that correspond to each record (residual) for  $T = 0.1$  s, 0.5 s, 1.0 s (left to right).

sized earthquakes of  $M_w \leq 5.7$ , which constitute 90% of the data we used, may show directivity effects. However, the azimuthal variation of rupture directivity effects is gradual over the  $\pm 90^\circ$  range in the strike-parallel directions ( $0^\circ$  and  $180^\circ$ ), while that from radiation pattern is more rapid within  $\pm 45^\circ$  range along strike-parallel ( $0^\circ$  and  $180^\circ$ ) and perpendicular directions ( $-90^\circ$  and  $90^\circ$ ). The empirical radiation pattern we show in Fig. 1, averaged over several strike-slip events, could be effected by rupture directivity of a few events. Although not discussed here, such events are flagged as those deviating significantly from the radiation pattern, and can be investigated for possible near-source effects.

For reference, we overlay the theoretical far-field S-wave radiation pattern ( $AS = \sqrt{F_{SH}^2 + F_{SV}^2}$ ), zero-centered and standardized, as the blue curve in Fig. 1. The theoretical far-field S-wave amplitudes for point-source dislocation in a homogenous half-space,  $F_{SH}$  and  $F_{SV}$ , are estimated for each record using the Aki and Richards<sup>6</sup> formulae. These formulae require parametric information on the rupture focal mechanism<sup>2,3</sup> (i.e., strike, dip, rake, hypocentral depth), crustal S-wave velocity model to calculate the take-off angles, epicentral distance, and azimuth of the recording station with respect to event epicentre<sup>2,3</sup>. Instead of an actual crustal velocity model, we used a take-off angle table<sup>38</sup> provided by the Japanese Meteorological Agency. Although  $AS$  (as with  $\sqrt{F_{SH}^2 + F_{SV}^2}$ ) are all positive values, these were zero-centered and standardized for visualization in Fig. 1. Clearly, the theoretical and empirical amplitudes show identical azimuthal dependence.

While Fig. 1 shows the evidence of S-wave radiation patterns for strike-slip events from both the KiK-net and NGA-West2 datasets, Fig. 2 presents similar plots for normal (1468 records from 64 events in M3.5–M6.0), reverse (2747 records from 198 events in M3.5–M6.0), and oblique (1864 records from 102 events of M3.5–M5.5) faulting events in the KiK-net dataset (including six events larger than M6.0). Since the global NGA-West2 dataset contains only large magnitude normal and reverse faults from diverse tectonic regions across the world, the coherency between theoretical and observed radiation patterns is not as clear as with the numerous smaller events of the Japanese KiK-net dataset (see Fig. 3 top-panel for data distribution).

The theoretical far-field S-wave radiation pattern, formulated for a point-source dislocation in homogenous, isotropic half-space, is deterministic and frequency-independent. Of course, these formulae cannot be used to

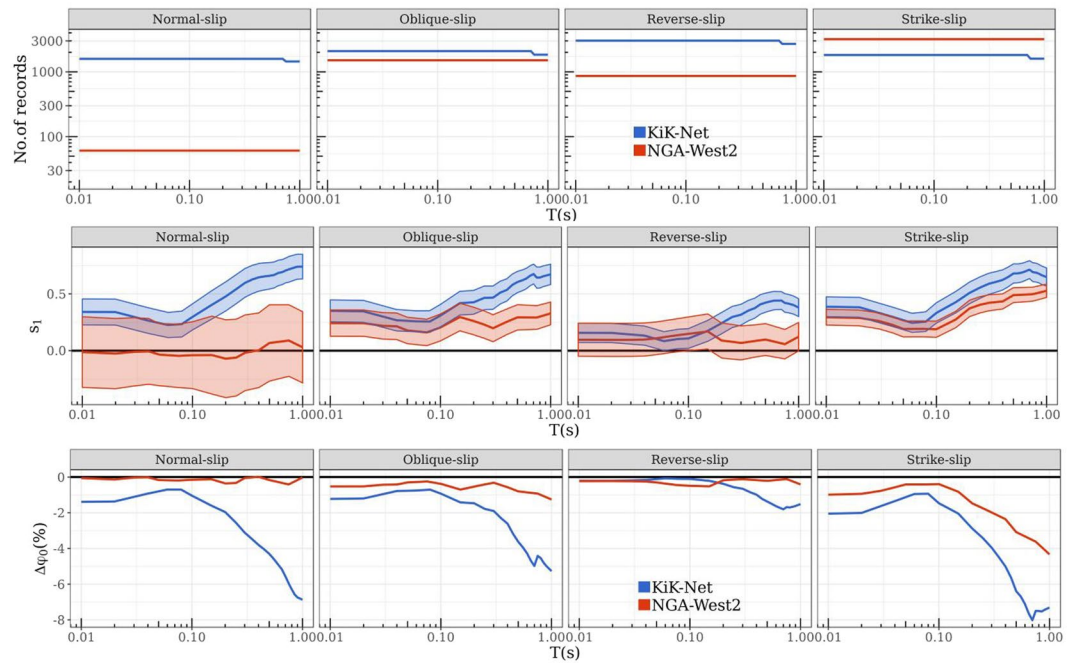


**Figure 3.** Calibration of style-of-faulting and period-dependent ( $T = 0.01$  s– $1.0$  s) linear relationships between theoretical far-field S-wave radiation amplitudes (AS) and aleatoric residuals ( $\delta WS_{e,s}$ ). Top panels: the (decreasing) number of records with increasing  $T$  at  $R \leq 100$  km of oblique, normal, reverse, and strike-slip events in the KiK-net (blue) and NGA-West2 (red) datasets. Middle panels: the estimated period-dependent  $s_1$  (with 95% confidence interval) of equation (2), which quantifies the presence of S-wave radiation patterns in ground-shaking residuals. Bottom panels: the reduction in the ground-shaking variability ( $\phi_0$ ) with the removal of the S-wave radiation pattern through the linear relationship.

model high frequency S-wave radiation pattern, where the complex crustal heterogeneities no longer qualify the propagation medium as a homogenous, isotropic half-space. We treat the theoretical pattern only as a *scale* to measure the transition of observed radiation between isotropic and anisotropic patterns. In this setup, the mismatch between the theoretical (blue lines in Figs 1 and 2) and empirical radiation patterns (red lines Figs 1 and 2) is maximum at short period PSA (Figs 1 and 2,  $T = 0.1$  s), which are analogues to high-frequency S-wave amplitudes. Moving towards longer periods (Figs 1 and 2,  $T = 0.5$  and  $1.0$  s), the agreement between the empirical and theoretical patterns improves, which indicates the characteristic transition from stochastic to deterministic phenomenon. Despite using data from scores of earthquakes across Japan and southern California, where crustal structures are known to be highly complex and heterogeneous, the theoretical idealizations appear to work surprisingly well – at least for low S-wave frequencies.

### Transition from Stochastic to Deterministic Phenomenon

Following the non-parametric analyses, we derived parametric models aiming to extract the S-wave radiation anisotropy from the ground-shaking residuals, and reintroduce anisotropic adjustments into the isotropic prediction models. For each dataset<sup>2,3</sup> independently, using a linear mixed-effects regression algorithm (lmer)<sup>32</sup>, we fit a simple, linear relation between the theoretical far-field S-wave radiation amplitudes and the residuals from isotropic ground-shaking models<sup>33,34</sup>. In equation (2),  $s_0$  is the intercept and  $s_1$  is the slope. Both  $s_0$  and  $s_1$  are set to vary with style-of-faulting (i.e., oblique, normal, reverse, strike-slip) in the mixed-effects regressions.

$$\delta WS_{e,s} = s_0 + s_1 \cdot AS_{e,s} \quad (2)$$

The top panels of Fig. 3 show the number of residuals/record used in deriving the  $s_1$  (and  $s_0$ ) values for the range  $T = 0.01$  s to  $1.0$  s for each style-of-faulting and dataset. Most of the NGA-West2 data is constituted by strike-slip and oblique-slip events, while the distribution is more even in KiK-net dataset – the style-of-faulting dependent values of  $s_1$  (and  $s_0$ ), estimated as random-effects in an lmer<sup>32</sup> of equation (2), is to account for such dataset imbalances.

There is a reason we limit our analyses to the period range  $T = 0.01$ – $1$  s. The KiK-net strong-motion dataset<sup>3</sup> we used is the product of an automatic processing of  $\sim 150,000$  seismograms from the NIED KiK-net database<sup>25</sup>, and is specifically built for engineering ground-shaking (PSA) studies such as ours<sup>33</sup>. Only through such automatic processing algorithms, it is possible to compile large datasets with thousands of records. However, the limitation of automatic processing is that we are required to apply a strict high-pass frequency filtering<sup>39</sup> criterion to discard records with limited usable low-frequency content. Consequently, the number of usable KiK-net<sup>3</sup> records drops rapidly for periods longer than  $T = 1$  s. The NGA-West2 dataset<sup>2</sup> on the other hand, is a product of manual processing of seismograms from active shallow crustal earthquakes, and therefore allows a wider usable period

range of  $T = 0.01\text{--}10$  s. However, to maintain consistency across datasets, we limited our investigation only in the period range  $T = 0.01\text{--}1$  s. Further details on data selection are available in the relevant articles elaborating on the development of Ground-Motion Prediction Equations<sup>33,34</sup> that we used in this study.

**Frequency Dependence of Radiation Pattern.** The agreement between theoretical and empirical radiation patterns is period ( $T$ ) dependent. In the middle panels of Fig. 3, considering  $s_1$  as a measure of correlation between empirical and theoretical patterns, and approximating  $f_{\text{osc}} (1/T)$  as S-wave frequencies, the monotonically increasing trend of  $s_1$  from  $T = 0.1$  s to 1.0 s ( $f_{\text{osc}} = 1\text{--}10$  Hz) can be interpreted as the transition of the S-wave radiation pattern from a stochastic to a deterministic process, which supports earlier findings<sup>17</sup>. Strike-slip events (Fig. 3, middle-right panel) from both datasets exhibit best the transition regime of the S-wave radiation patterns in their residuals – with statistically significant (as shown by its 95% confidence interval) estimates of  $s_1$ . Normal, oblique, and reverse-slip events of the KiK-net show a clear trend as well, while there is very little data from normal-slip events in NGA-West2.

The efficiency of equation (2) in capturing and removing S-wave radiation anisotropy from the  $\delta WS_{e,s}$  is measured in terms of the reduction in prediction variance ( $\phi_0$ , the standard deviation of  $\delta WS_{e,s}$ ) of the parent ground-shaking models<sup>33,34</sup>. In the bottom panels of Fig. 3, we see up to 8% reduction in  $\phi_0$  for normal, oblique, and strike-slip events of the KiK-net dataset. Such reductions in the ground-shaking prediction variance are highly sought in Probabilistic Seismic Hazard Assessment<sup>40</sup>. Reverse-slip events do not show as much reduction – we discuss this in the following section.

**Distance Dependence of Radiation Pattern.** A recent study<sup>41</sup> asserted that, for large earthquakes, radiation pattern controls the near-source saturation of ground-shaking. A few earlier studies<sup>12,13,22</sup>, based on small to moderate sized earthquakes, observed that the four-lobbed radiation pattern remains intact up to 40 km, beyond which seismic wave scattering and diffraction in the heterogeneous crust distorts the radiation pattern<sup>42</sup>. While these studies were based on a few strike-slip events in a locality, we extend the investigation with several more strike, normal, reverse, and oblique-slip events all over Japan.

In Fig. 3, the frequency-dependence of radiation pattern for each style-of-faulting is estimated and presented using recordings with  $R \leq 100$  km. While Fig. 4 presents the distance-dependence of radiation pattern within this 100 km range, and up to 200 km, for normal, oblique, reverse, and strike-slip events at  $T = 0.1, 0.5$  and 1 s. To demonstrate the distance-dependence, we estimate the  $s_1$  (equation 2) within each moving distance window of 0–30 km, 10–40 km, 20–50 km, and so on up to 200 km. For brevity, we present the results only for the KiK-net dataset.

Figure 4 shows that the period- and distance-dependence of S-wave radiation pattern is strongly dependent on the style-of-faulting of the events. Firstly, for strike-slip events, the  $s_1$  values at  $T = 0.5$  s are significant (95% confidence intervals) up to 100 km. For long period PSAs ( $T = 1$  s), which we consider comparable to low frequency S-wave amplitudes, we observe that significant  $s_1$  estimates persist up to 200 km. On the other hand, normal and oblique-slip events show a much earlier decay in correlation starting at  $R \sim 20\text{--}40$  km, depending on the frequency.

Reverse-slip events are peculiar in a few aspects. For instance, despite being the largest contributors to the KiK-net dataset in terms of number of events and records, they show a weaker correlation (smaller  $s_1$  in Fig. 3) values, and lesser reduction in aleatory variability, than other style-of-faulting events. At the same time, the distance-dependent decay (for  $T = 1$  s in Fig. 4) starts to be significant at around 100 km – much later than normal and oblique-slip events. Empirical<sup>43,44</sup> and simulation<sup>45</sup> based studies showed that the hanging-wall effects of reverse-slip events may persist up to 100 km, and are sensitive to magnitude, dip, and depth to top-of-rupture plane. Observations from M7.6 Chi-Chi (Taiwan), M6.7, Northridge (New-Zealand), M6.3, L'Aquila (Italy), and M7.9, Wenchuan (China) support these simulations<sup>45</sup>; wherein, equidistant ground-shaking intensities (PSAs) on the hanging-wall could be three times larger than those on the foot-wall side of the rupture. Such large variability in observed ground-shaking due to effects finite-fault geometry (trapping of waves in the hanging-wall *wedge*), along with crustal heterogeneity (from crustal fractures), warrants a more detailed region-dependent investigation of reverse-slip events.

Based on Fig. 4, we suggest that the distance-dependence of S-wave radiation pattern integrity is also dependent on the focal-mechanism and spectral period ( $T$ ), and vice-versa. While earlier studies suggested the radiation pattern is intact only up to 40 km, we find that for strike-slip events the range could be much longer, especially for long period PSAs (low frequency S-wave amplitudes). It is important to note that, focal mechanisms are characterized by tectonic environments, such as maximum shear stress orientation<sup>46</sup>. The distance dependence we observe to be characteristic of focal mechanisms, could as well be related to regional differences (within Japan)<sup>47</sup> in scattering and absorption<sup>12,39</sup>. With this in mind, we intend a more thorough investigation of the magnitude, depth and crustal structure dependencies of  $s_1$ . For interested readers, all the data plotted in Figs 1–4 are provided as electronic supplements for further investigations.

## Anisotropic Ground-Shaking Predictions

For a new event, given its rupture focal-mechanism and regional S-wave crustal velocity structure (or take-off angle table)<sup>38</sup>, the theoretical S-wave radiation amplitudes (AS) in its vicinity can be estimated, which can then be translated into anisotropic ground-shaking adjustments compatible with the isotropic ground-shaking prediction models<sup>33,34</sup>. We use the period-, distance- and style-of-faulting dependent coefficients  $s_0$  and  $s_1$  derived from the Japanese KiK-net dataset<sup>3</sup> (shown in Fig. 4) to predict the radiation patterns of four well-recorded events available in the dataset (Table 1). Instead of comparing observed and predicted PSAs for each event at  $T = 0.1, 0.5$  and 1 s, Fig. 5 compares the predicted anisotropic amplification/attenuation (equation 2 with coefficients in Fig. 4) against the observed deviation (i.e., residual  $\delta WS_{e,s}$  at each surface site  $s$  for event  $e$ ) from isotropic,



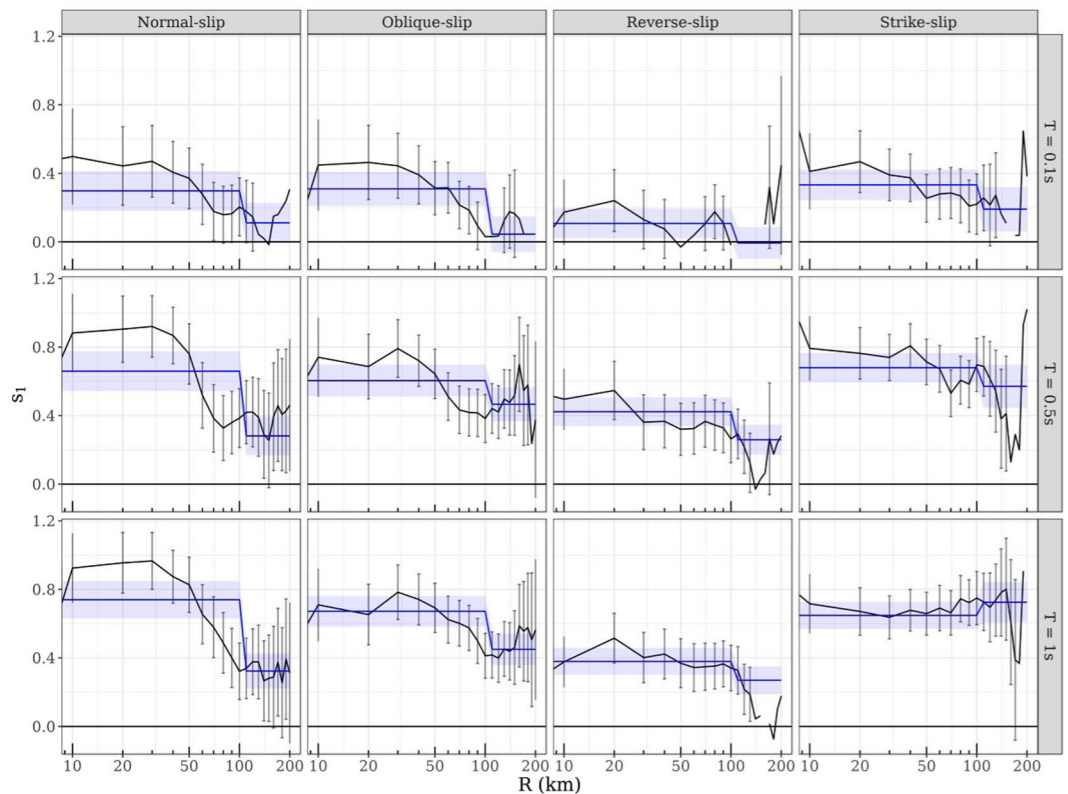


**Figure 4.** Distance dependence of radiation pattern for normal, oblique, reverse, and strike-slip events in the KiK-net dataset at  $T = 0.1, 0.5$  and  $1$  s: Correlation between the theoretical and empirical radiation patterns is measured in terms of  $s_1$  in equation (2), for distance bins 0–30 km, 10–40 km, 20–50 km and so on. The solid black line and error bars depict bin-wise  $s_1$  and 95% confidence estimates respectively. The solid blue line and error ribbon depicts the  $s_1$  and its 95% confidence interval estimated for distance bins  $R \leq 100$  km and  $R > 100$  km. Note that the blue lines assume values shown in middle panel of Fig. 3. Evidently the period and distance-dependence of S-wave radiation pattern is also dependent on the style-of-faulting of the events. While the strike-slip events show good correlation with theoretical expectation for epicentral distances larger than 100 km as well for  $T = 1$  s, normal and oblique-slip events show a much earlier decay starting at  $R \sim 40$  km.

Event	Style-of-faulting	Focal-mechanism (dip, rake, strike)	Location (WGS84)	Origin (JST)	$M_w$	Depth (km)
NM	Normal	(54°, -120°, 69°)	(130.89°E, 33.37°N)	25/06/2009 23:04	4.5	8
OB	Oblique	(88°, 35°, 332°)	(137.11°E, 35.76°N)	27/07/2004 00:55	4.2	8
RS	Reverse	(51°, 63°, 88°)	(138.50°E, 34.79°N)	11/08/2009 05:07	6.2	20
SS	Strike	(90°, -175°, 85°)	(137.70°E, 35.91°N)	13/06/2008 11:22	4.3	20

**Table 1.** Event metadata of the four events shown in Fig. 5.

event- and site-specific PSA predictions by the KiK-net based ground-shaking model<sup>33</sup>. Generic, event- and site-independent isotropic PSA predictions can be estimated using only the fixed-effects of equation (1), whose regression coefficients are available as an online resource<sup>33</sup>. These generic predictions can then be adjusted to event- and site-specific predictions<sup>30</sup> using the random-effects (is  $\delta B_e$  and  $\delta S_2 S_s$ ) provided in the electronic supplements of this article, which also contain the residuals ( $\delta WS_{e,s}$ ).

We choose four events with more than 30 recordings at  $R \leq 200$  km, and predict the S-wave radiation pattern in a 200 km radius around the rupture epicenter. The event metadata for the four events is provided in Table 1, while the event- and site-specific random-effects are provided in the electronic supplements. The colors in Fig. 5 reflect anisotropic increases (red) and decreases (blue) in the ground-shaking with respect to the isotropic event- and site-specific predictions in the region. The predicted radiation patterns are overlain by the locations (markers) of the recording surface sites, which are color coded for observed  $e^{\delta WS_{e,s}}$ , to indicate larger or smaller than predicted isotropic event- and site-specific ground-shaking. Essentially, we compare the anisotropic amplifications from an average model derived over several events in the Japanese KiK-net data with the anisotropic observations

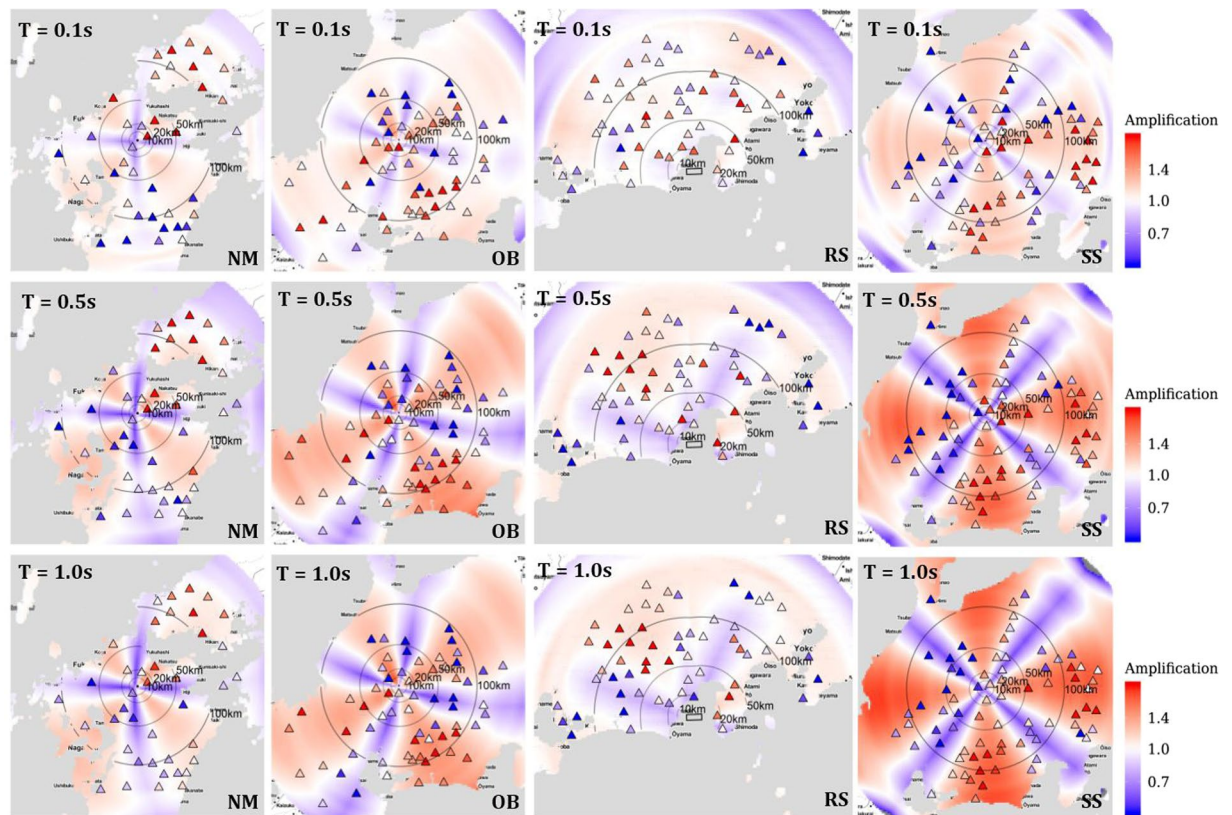


**Figure 5.** Period-, distance- and style-of-faulting dependent anisotropic ground-shaking amplification predictions for four events in Japan (NM: Normal, OB: Oblique, RS: Reverse, and SS: Strike-slip from left to right panels), for periods  $T = 0.1, 0.5$  and  $1$  s (top-to-bottom panels). Each panel shows the  $R \leq 200$  km region (with 10, 20, 50, 100 km contour lines) around the rupture trace, with color coding to reflect anisotropic increases (red)/decreases (blue) in ground-shaking with respect to the isotropic predictions, as a result of including the S-wave radiation pattern in empirical ground-shaking predictions. Overlying markers indicate the locations of recording sites, which are also color coded to reflect systematically higher (red) or lower (blue) than median isotropic ground-shaking model predictions. Wherever the background colors coincide with marker colors, the prediction model captures the observed anisotropic spatial variability of the ground-shaking reasonably well.

for well-recorded events, and this appears to work quite well. Qualitatively, the anisotropic ground-shaking predictions capture the observed anisotropy very well, which is of course period- and distance- dependent for each style-of-faulting. Quantitatively though, where the calibrated model suggests S-wave intensities that are 0.7-fold to 1.4-fold the median isotropic event- and site-specific ground-shaking predictions, the observations ( $e^{\delta^{WS_{e,s}}}$ ) show much stronger anisotropy of the order of 0.5-fold to 2-fold. Note that our models capture the ‘average’ S-wave radiation pattern over several sparsely recorded  $M3.4$  to  $M6.9$  events that are scattered across Japan. This means that some events (in some regions of Japan) show stronger correlations between the theoretical S-wave radiation patterns and the observed anisotropy of the ground-shaking, while others fall short. In addition, near-source effects such as the directivity and hanging-wall effects, crustal heterogeneities, and complex 2D/3D site-responses could be exaggerating the mismatch between the observations and predictions.

Figures 1 and 2 show a very weak correspondence between theoretical and observed radiation patterns at  $T = 0.1$  s, while Figs 3 and 4 show that the  $s_1$  values are either small or insignificant at  $T = 0.1$  s. Consequently, our predictions in the top-panels of Fig. 5, corresponding to  $T = 0.1$  s, produce relatively weak anisotropy, as indicated by the fainter colors (white meaning no anisotropy). Not to mention, theoretical far-field S-wave radiation equations cannot be applied at short periods ( $T = 0.1$  s), where the assumptions of crustal homogeneity and isotropy do not hold anymore.

### Implications in Seismic Ground-Shaking Studies

S-wave radiation pattern is an extensively studied phenomenon in seismology. They have been repeatedly observed and quantified from observed S-wave amplitudes of a few well-recorded strike-slip events in the Fourier domain, or sometimes Peak Ground Acceleration and Velocity. However, within engineering seismology, they have never been quantified over large datasets of PSAs (Pseudo-Spectral Accelerations) from several normal, oblique, reverse, and strike-slip events – PSAs are the standard ground-shaking intensity measures applied in structural design codes, probabilistic seismic hazard and risk assessments, and ShakeMaps. The reasons for this include the limited spatial density of strong-motion networks to observe the patterns for any single event, and the



dominance of other ground-shaking attenuation processes. In this study, we have revealed the imprint of S-wave radiation pattern in the regression residuals of existing, isotropic ground-shaking prediction models.

The novelty of our approach is to systematically remove the dominant physical effects from the recorded ground-shaking data, and to reorient the strong-motion network to emulate a complete azimuthal (0–360°) and distance coverage (0–200 km). The S-wave radiation pattern becomes evident, with its characteristic transition from a stochastic at high frequencies (short period PSAs) to a deterministic at low frequencies (long period PSAs) phenomenon. The transition appears to depend also on the events' style-of-faulting and distance to the recording surface sites. We calibrate a period-, distance- and style-of-faulting dependent empirical model (equation 2) correlating theoretical far-field radiation coefficients with the empirical ground-shaking model residuals.

Our empirical radiation pattern models are simple and practical. The coefficients  $s_0$  and  $s_1$  of equation (2), derived from the KiK-net and NGA-West2 datasets, can be applied to the respective isotropic ground-shaking prediction models<sup>33,34</sup> as in:  $\log(\text{PSA}_{\text{anisotropic}}) = \log(\text{PSA}_{\text{isotropic}}) + s_0 + s_1 \cdot \text{AS}$ . These adjustment factors have an impact on ground-shaking maps; with at least  $\pm 40\%$  change in the isodistant predictions, depending on the site azimuth and distance relative to the event epicentre. In complement, the prediction variance  $\phi_0$  is reduced by up to 8% for the KiK-net dataset based ground-shaking model.

Regional dependence<sup>39,46,47</sup> of adjustment factors ( $s_0$  and  $s_1$  of equation 2) is an issue worth investigating, given that we do observe some event-to-event (or regional) variability - but that would require a more complex treatment of crustal heterogeneities. Our method, producing average adjustment factors, aims to balance model complexity and ease of applicability, so that anisotropic adjustment factors can be estimated for any empirical ground-shaking prediction model.

Our study intends a new approach to the inclusion of style-of-faulting effects in empirical ground-shaking prediction models. For instance, several ground-shaking models<sup>4,5</sup> derived from the NGA-West2<sup>2</sup> and RESORCE<sup>31</sup> datasets (used in USGS<sup>48</sup> and SHARE<sup>49</sup> hazard maps) propose average isotropic, style-of-faulting and frequency-dependent adjustment factors. These factors were shown to vary considerably from one model to another and were not representative of any clear physical phenomenon<sup>50</sup>. While some studies could not constrain these adjustment factors<sup>29,51</sup>, others could only derive them for large earthquakes<sup>4</sup>. We demonstrate here that the lack of robustness in handling the style-of-faulting is in-fact from the assumption of averaged distance-independent isotropy, where distance and style-of-faulting dependent anisotropy appears to be prevalent.

From the lack of detailed knowledge of wave-propagation and rupture processes, physics-based broadband ground-shaking simulations<sup>52</sup> usually consider isotropic radiation patterns that arise from the average of the theoretical radiation patterns over a suitable range of azimuth and take-off angles<sup>53</sup> for high-frequency S-waves. Some recent developments have reproduced the homogenization of radiation pattern effects at higher frequencies using heterogeneous short-length scaled-rupture mechanisms<sup>54</sup> or deterministic numerical modeling in three-dimensional heterogeneous Earth crust models. The empirical evidence presented in this study can be used to calibrate these simulations and the parameters that describe the medium-scattering properties and small-scale random-slip distributions.

We foresee a need for reappraisal of some other engineering seismology issues as well; such as the impact of incident S-wave azimuth on variability of soil response, the P-wave and S-wave intensity correlations at forward stations used in early warning systems<sup>13</sup>, landslide triggering from seismic actions, risk assessment of spatially extended infrastructures<sup>55</sup>, and ShakeMaps<sup>1</sup> for rapid responses. Moreover, all of these products rely on ground-shaking maps with spatially cross-correlated predictions, which despite their wide utility<sup>56</sup> in seismic risk assessment, and reliance on spatial cross-correlation models<sup>57</sup> derived from residuals of ground-shaking models, have not seen any great revisions in the past few years. Along with the upgrade of existing ground-shaking prediction models, new models from newer and larger datasets<sup>58,59</sup> providing both Fourier and PSA amplitudes can improve upon our study. Ultimately, the large ground-shaking datasets we have compiled over the last decade are the tools we needed to revisit the old hypotheses, made when data was once scarce.

## Methods

The NGA-West2<sup>2</sup>, KiK-net datasets<sup>3</sup>, and take-off angle tables<sup>38</sup> used in this study are publicly available. As an electronic supplement, we provide an extract of the KiK-net dataset with all relevant data and model coefficients of equation (2). The peer-reviewed and published isotropic ground-shaking models<sup>33,34</sup> were developed using either the R-software<sup>60</sup> or a multi-step mixed-effects regression procedure described in the relevant publications<sup>34</sup>. The equations used to calculate the far-field S-wave radiation coefficients were developed by Aki and Richards<sup>6</sup>.

## References

- Wald, D. J. *et al.* TriNet “ShakeMaps”: Rapid generation of peak ground motion and intensity maps for earthquakes in southern California. *Earthquake Spectra* **15**, 537–555 (1999).
- Ancheta, T. D. *et al.* NGA-West2 database. *Earthquake Spectra* **30**, 989–1005 (2014).
- Dawood, H. M., Rodriguez-Marek, A., Bayless, J., Goulet, C. & Thompson, E. A Flatfile for the KiK-net Database Processed Using an Automated Protocol. *Earthquake Spectra* **32**, 1281–1302 (2016).
- Gregor, N. *et al.* Comparison of NGA-West2 GMPEs. *Earthquake Spectra* **30**, 1179–1197 (2014).
- Douglas, J. *et al.* Comparisons among the five ground-motion models developed using RESORCE for the prediction of response spectral accelerations due to earthquakes in Europe and the Middle East. *Bulletin of earthquake engineering* **12**, 341–358 (2014).
- Aki, K. & Richards, P. G. *Quantitative Seismology, Vol. 2.* (WH Freeman, San Francisco, 1980).
- Liu, H.-L. & Helmberger, D. V. The 23: 19 aftershock of the 15 October 1979 Imperial Valley earthquake: more evidence for an asperity. *Bulletin of the Seismological Society of America* **75**, 689–708 (1985).
- Vidale, J. E. Influence of focal mechanism on peak accelerations of strong motions of the Whittier Narrows, California, earthquake and an aftershock. *Journal of Geophysical Research: Solid Earth* **94**, 9607–9613 (1989).

9. Campbell, K. W. & Bozorgnia, Y. Empirical-Analysis of Strong Ground Motion from the 1992 Landers, California, Earthquake. *Bulletin of the Seismological Society of America* **84**, 573–588 (1994).
10. Sirovich, L. A case of the influence of radiation pattern on peak accelerations. *Bulletin of the Seismological Society of America* **84**, 1658–1664 (1994).
11. Douglas, J. A *Critical Reappraisal of Some Problems in Engineering Seismology* Doctor of Philosophy thesis, Imperial College of Science, *Technology and Medicine* (2001).
12. Takemura, S., Furumura, T. & Saito, T. Distortion of the apparent S-wave radiation pattern in the high-frequency wavefield: Tottori-Ken Seibu, Japan, earthquake of 2000. *Geophysical Journal International* **178**, 950–961 (2009).
13. Takemura, S., Kobayashi, M. & Yoshimoto, K. Prediction of maximum P- and S-wave amplitude distributions incorporating frequency- and distance-dependent characteristics of the observed apparent radiation patterns. *Earth, Planets and Space* **68**, 166 (2016).
14. Sawazaki, K., Sato, H. & Nishimura, T. Envelope synthesis of short-period seismograms in 3-D random media for a point shear dislocation source based on the forward scattering approximation: Application to small strike-slip earthquakes in southwestern Japan. *Journal of Geophysical Research: Solid Earth* **116** (2011).
15. Takenaka, H., Mamada, Y. & Futamura, H. Near-source effect on radiation pattern of high-frequency S waves: strong SH–SV mixing observed from aftershocks of the 1997 Northwestern Kagoshima, Japan, earthquakes. *Physics of the Earth and Planetary Interiors* **137**, 31–43 (2003).
16. Castro, R. R., Franceschina, G., Pacor, F., Bindi, D. & Luzi, L. Analysis of the frequency dependence of the S-wave radiation pattern from local earthquakes in central Italy. *Bulletin of the Seismological Society of America* **96**, 415–426 (2006).
17. Imperatori, W. & Mai, P. M. Broad-band near-field ground motion simulations in 3-dimensional scattering media. *Geophysical Journal International* **192**, 725–744 (2012).
18. Pulido, N. & Kubo, T. Near-fault strong motion complexity of the 2000 Tottori earthquake (Japan) from a broadband source asperity model. *Tectonophysics* **390**, 177–192 (2004).
19. Pitarka, A., Somerville, P., Fukushima, Y., Uetake, T. & Irikura, K. Simulation of near-fault strong-ground motion using hybrid Green's functions. *Bulletin of the Seismological Society of America* **90**, 566–586 (2000).
20. Satoh, T. Generation method of stochastic Green's function considering into surface waves and scattering waves using records of moderate-size interplate earthquakes along the Sagami Trough. *Journal of Structural and Construction Engineering* **79**, 1589–1599 (in Japanese with English abstract) (2014).
21. Satoh, T. Radiation pattern and  $f_{max}$  of the Tottori-ken Seibu earthquake and the aftershocks inferred from KiK-net strong motion records. *Journal of Structural and Construction Engineering*, 25–34 (in Japanese with English abstract) (2002).
22. Kobayashi, M., Takemura, S. & Yoshimoto, K. Frequency and distance changes in the apparent P-wave radiation pattern: effects of seismic wave scattering in the crust inferred from dense seismic observations and numerical simulations. *Geophysical Journal International* **202**, 1895–1907 (2015).
23. Code, P. Eurocode 8: Design of structures for earthquake resistance-part 1: general rules, seismic actions and rules for buildings. *Brussels: European Committee for Standardization* (2005).
24. Council, B. S. S. The 2000 NEHRP Recommended Provisions for New Buildings and Other Structures, Part I (Provisions) and Part II (Commentary). *FEMA* **368**, 369 (2000).
25. Okada, Y. *et al.* Recent progress of seismic observation networks in Japan—Hi-net, F-net, K-NET and KiK-net—. *Earth, Planets and Space* **56**, xv–xxviii (2004).
26. Hauksson, E. *et al.* Southern California seismic network: Caltech/USGS element of TriNet 1997–2001. *Seismological Research Letters* **72**, 690–704 (2001).
27. Housner, G. & Brady, A. Natural periods of vibration of buildings. *Journal of the Engineering Mechanics Division* **89**, 31–68 (1963).
28. Frankel, A. Decay of S-wave amplitudes with distance for earthquakes in the Charlevoix, Quebec, area: Effects of radiation pattern and directivity. *Bulletin of the Seismological Society of America* **105**, 850–857 (2015).
29. Kotha, S. R., Bindi, D. & Cotton, F. Partially non-ergodic region specific GMPE for Europe and Middle-East. *Bulletin of Earthquake Engineering* **14**, 1245–1263 (2016).
30. Kotha, S. R., Bindi, D. & Cotton, F. From ergodic to region- and site-specific probabilistic seismic hazard assessment: Method development and application at European and Middle Eastern sites. *Earthquake Spectra* **33**, 1433–1453, <https://doi.org/10.1193/081016EQS.130M> (2017).
31. Akkar, S. *et al.* Reference database for seismic ground-motion in Europe (RESORCE). *Bulletin of earthquake engineering* **12**, 311–339 (2014).
32. Bates, D., Mächler, M., Bolker, B. & Walker, S. Fitting linear mixed-effects models using lme4. *arXiv preprint arXiv:1406.5823* (2014).
33. Kotha, S. R., Cotton, F. & Bindi, D. A new approach to site classification: Mixed-effects Ground Motion Prediction Equation with spectral clustering of site amplification functions. *Soil Dynamics and Earthquake Engineering*, <https://doi.org/10.1016/j.soildyn.2018.01.051> (2018).
34. Boore, D. M., Stewart, J. P., Seyhan, E. & Atkinson, G. M. NGA-West2 equations for predicting PGA, PGV, and 5% damped PSA for shallow crustal earthquakes. *Earthquake Spectra* **30**, 1057–1085 (2014).
35. Boore, D. M., Watson-Lamprey, J. & Abrahamson, N. A. Orientation-independent measures of ground motion. *Bulletin of the Seismological Society of America* **96**, 1502–1511 (2006).
36. Bora, S. S., Scherbaum, F., Kuehn, N. & Stafford, P. On the relationship between Fourier and response spectra: Implications for the adjustment of empirical ground-motion prediction equations (GMPEs). *Bulletin of the Seismological Society of America* **106**, 1235–1253 (2016).
37. Pacor, F., Gallovič, F., Puglia, R., Luzi, L. & D'Amico, M. Diminishing high-frequency directivity due to a source effect: Empirical evidence from small earthquakes in the Abruzzo region, Italy. *Geophysical Research Letters* **43**, 5000–5008 (2016).
38. JMA. *Travel time table, take-off angle table and seismic velocity structure files*, [http://www.data.jma.go.jp/svd/eqev/data/bulletin/catalog/appendix/trtime/trt\\_e.html](http://www.data.jma.go.jp/svd/eqev/data/bulletin/catalog/appendix/trtime/trt_e.html) ( ).
39. Boore, D. M. & Bommer, J. J. Processing of strong-motion accelerograms: needs, options and consequences. *Soil Dynamics and Earthquake Engineering* **25**, 93–115 (2005).
40. Bommer, J. J. & Abrahamson, N. A. Why do modern probabilistic seismic-hazard analyses often lead to increased hazard estimates? *Bulletin of the Seismological Society of America* **96**, 1967–1977 (2006).
41. Dujardin, A., Causse, M., Berge-Thierry, C. & Hollender, F. Radiation Patterns Control the Near-Source Ground-Motion Saturation Effect. *Bulletin of the Seismological Society of America*, <https://doi.org/10.1785/0120180076> (2018).
42. Takemura, S., Kobayashi, M. & Yoshimoto, K. High-frequency seismic wave propagation within the heterogeneous crust: effects of seismic scattering and intrinsic attenuation on ground motion modelling. *Geophysical Journal International* **210**, 1806–1822 (2017).
43. Abrahamson, N. & Somerville, P. Effects of the hanging wall and footwall on ground motions recorded during the Northridge earthquake. *Bulletin of the Seismological Society of America* **86**, S93–S99 (1996).
44. Chang, T.-Y., Cotton, F., Tsai, Y.-B. & Angelier, J. Quantification of hanging-wall effects on ground motion: some insights from the 1999 Chi-Chi earthquake. *Bulletin of the Seismological Society of America* **94**, 2186–2197 (2004).
45. Donahue, J. L. & Abrahamson, N. A. Simulation-based hanging wall effects. *Earthquake Spectra* **30**, 1269–1284 (2014).
46. Terakawa, T. & Matsu'Ura, M. The 3-D tectonic stress fields in and around Japan inverted from centroid moment tensor data of seismic events. *Tectonics* **29** (2010).

47. Carcolé, E. & Sato, H. Spatial distribution of scattering loss and intrinsic absorption of short-period S waves in the lithosphere of Japan on the basis of the Multiple Lapse Time Window Analysis of Hi-net data. *Geophysical Journal International* **180**, 268–290 (2010).
48. Petersen, M. D. *et al.* The 2014 United States national seismic hazard model. *Earthquake Spectra* **31**, S1–S30 (2015).
49. Woessner, J. *et al.* The 2013 European Seismic Hazard Model: key components and results. *Bulletin of Earthquake Engineering* **13**, 3553–3596, <https://doi.org/10.1007/s10518-015-9795-1> (2015).
50. Bommer, J. J., Douglas, J. & Strasser, F. O. Style-of-faulting in ground-motion prediction equations. *Bulletin of Earthquake Engineering* **1**, 171–203 (2003).
51. Bindi, D. *et al.* Application-driven ground motion prediction equation for seismic hazard assessments in non-cratonic moderate-seismicity areas. *Journal of Seismology* **21**, 1201–1218, <https://doi.org/10.1007/s10950-017-9661-5> (2017).
52. Graves, R. W. & Pitarka, A. Broadband ground-motion simulation using a hybrid approach. *Bulletin of the Seismological Society of America* **100**, 2095–2123 (2010).
53. Boore, D. M. & Boatwright, J. Average body-wave radiation coefficients. *Bulletin of the Seismological Society of America* **74**, 1615–1621 (1984).
54. Graves, R. & Pitarka, A. Kinematic ground-motion simulations on rough faults including effects of 3D stochastic velocity perturbations. *Bulletin of the Seismological Society of America* **106**, 2136–2153 (2016).
55. Kotha, S. R., Bazzurro, P. & Pagani, M. Effects of Epistemic Uncertainty in Seismic Hazard Estimates on Building Portfolio Losses. *Earthquake Spectra* **34**, 217–236 (2018).
56. Park, J., Bazzurro, P. & Baker, J. Modeling spatial correlation of ground motion intensity measures for regional seismic hazard and portfolio loss estimation. *Applications of statistics and probability in civil engineering*, 1–8 (2007).
57. Loth, C. & Baker, J. W. A spatial cross-correlation model of spectral accelerations at multiple periods. *Earthquake Engineering & Structural Dynamics* **42**, 397–417 (2013).
58. Lanzano, G. *et al.* The pan-European engineering strong motion (ESM) flatfile: compilation criteria and data statistics. *Bulletin of Earthquake Engineering*, 1–22 (2018).
59. Bindi, D. *et al.* The pan-European engineering strong motion (ESM) flatfile: consistency check via residual analysis. *Bulletin of Earthquake Engineering*, 1–20 (2018).
60. R: A language and environment for statistical computing (R Foundation for Statistical Computing, Vienna, Austria, 2010).

## Acknowledgements

We thank the two *anonymous* reviewers whose constructive criticism helped us improve the manuscript considerably. We would like to thank Eleonora Rivalta for her valuable insights. We extend our thanks to our colleagues at section 2.6: Seismic Hazard and Risk Dynamics of GeoForschungsZentrum Potsdam, for the regular discussions and feedbacks. This research is funded by the SIGMA2 consortium (EDF, CEA, PG&E, SwissNuclear, Areva, CEZ, CRIEPI) under grant – 2017–2021 (<http://www.sigma-2.net/>).

## Author Contributions

The conceptualization, methodology, presentation and revision of the study are the combined efforts of Sreeram Reddy Kotha, Fabrice Cotton, and Dino Bindi. The initial investigation, programming, visualization, and writing of the manuscript were performed by Sreeram Reddy Kotha. Other contributions to internal review and discussions are acknowledged.

## Additional Information

**Supplementary information** accompanies this paper at <https://doi.org/10.1038/s41598-018-37524-4>.

**Competing Interests:** The authors declare no competing interests.

**Publisher's note:** Springer Nature remains neutral with regard to jurisdictional claims in published maps and institutional affiliations.



**Open Access** This article is licensed under a Creative Commons Attribution 4.0 International License, which permits use, sharing, adaptation, distribution and reproduction in any medium or format, as long as you give appropriate credit to the original author(s) and the source, provide a link to the Creative Commons license, and indicate if changes were made. The images or other third party material in this article are included in the article's Creative Commons license, unless indicated otherwise in a credit line to the material. If material is not included in the article's Creative Commons license and your intended use is not permitted by statutory regulation or exceeds the permitted use, you will need to obtain permission directly from the copyright holder. To view a copy of this license, visit <http://creativecommons.org/licenses/by/4.0/>.

© The Author(s) 2019